Title

Uncovering the Relationship between Diameter and Height of Electrodeposited Lithium Protrusions in a Rigid Electrolyte

Journal

ACS Applied Energy Materials, 3(10)

ISSN

2574-0962

Authors

Ho, Alec S
Barai, Pallab
Maslyn, Jacqueline A
et al.

Publication Date

2020-10-26

DOI

10.1021/acsaem.0c01175

Peer reviewed

Uncovering the Relationship between Diameter and Height of Electrodeposited Lithium Protrusions in a Rigid Electrolyte

Alec S. Ho [a, b], *Pallab Barai* [c], *Jacqueline A. Maslyn* [a, b], *Louise Frenck* [a], *Whitney S. Loo* [a], *Dilworth Y. Parkinson* [d], *Venkat Srinivasan* [c], *Nitash P. Balsara* [a, b, e, *]

[a] Department of Chemical and Biomolecular Engineering, University of California, Berkeley, California 94720, USA

[b] Materials Sciences Division, Lawrence Berkeley National Laboratory, Berkeley, California, 94720, USA

[c] Argonne National Laboratory, Lemont, Illinois 60439, USA

[d] Advanced Light Source, Lawrence Berkeley National Laboratory, Berkeley, California 94720, USA

[e] Energy Technologies Area, Lawrence Berkeley National Laboratory, Berkeley, California 94720, USA

* Corresponding author. E-mail: nbalsara@berkeley.edu, Phone: 1-510-642-8973.

Abstract

A promising approach for enabling rechargeable batteries with significantly higher energy densities than current lithium-ion batteries is by deploying lithium metal anodes. However, the growth of lithium protrusions during charging presents significant challenges. Since these protrusions are often branched and filamentous in conventional liquid electrolytes, this problem is referred to in literature as the "dendrite problem". While solid electrolytes have the potential to solve this problem, protrusions grow in all electrolytes when the current density exceeds a critical value. Fundamentally understanding the formation is necessary to develop a rational approach for increasing the critical current density, but it is challenging due to the complex interplay between electrochemical and material properties. The diameters and heights of protrusions on lithium metal anodes stabilized by a rigid block copolymer electrolyte were measured in situ by synchrotron hard X-ray microtomography. The diameter of the shorting protrusions increased linearly with increasing electrolyte thickness. Further, a universal linear relationship between protrusion height and diameter of both shorting and non-shorting protrusions was observed. A model based on concentrated solution theory was used to establish the electrochemical and mechanical sources for our observations. The computational analysis indicates that elastic and plastic deformation of both the lithium metal and the polymer are important to describe protrusion growth. Both stress-induced current density effects due the deformation of the electrolyte near the protrusion and plastic deformation of lithium metal combine to give the counterintuitive result: the fastest-growing protrusions have the largest diameter.

KEYWORDS: *lithium metal; polymer electrolyte; lithium dendrite; protrusion morphology; X-ray tomography*

Introduction

There is continued interest in developing rechargeable batteries with energy densities that are higher than that of current lithium-ion batteries. One approach to develop such systems is to enable lithium metal anodes.[1–3] However, the growth of lithium protrusions from the metal anode during charging causes battery failure.[4–6] The consequences can be particularly catastrophic if the protrusion causes a short-circuit.[7,8] If conventional liquid electrolytes are used in lithium metal batteries, these protrusions are dendritic in nature, and this problem is referred to in literature as the "dendrite problem".[9,10] Several studies have shown that solid electrolytes can mechanically suppress lithium protrusion growth.[11–18] Despite these efforts, stopping the growth of lithium protrusions entirely remains an unmet challenge. The purpose of this study is to shed light on the fundamental underpinnings of lithium protrusion growth through a solid polymer electrolyte.

The theoretical understanding of suppressing protrusion growth mechanically began with the work of Monroe and Newman.[11,19,20] In conventional electrochemical systems with liquid electrolytes, the electrochemical potential at the electrode surface depends on temperature, pressure, composition, and the electrical state of the system.[21] When the current required for the electrochemical reaction is drawn from a solid electrolyte, the electrochemical potential is also affected by the stress in the electrolyte. At sufficiently small stress, the relationship between stress and strain in solids is linear, and this relationship is quantified by the elastic modulus. Monroe and Newman predicted that protrusion growth would be stopped if the modulus of the electrolyte were a factor of two higher than that of lithium metal. They also quantified the

relationship between stress in the electrolyte and the local current density at the tip of the protrusion. Several subsequent studies have built upon this model to characterize the crossover from planar to nonplanar electrodeposition in the presence of solid electrolytes.[22–25] These studies do not address the mechanism by which protrusions grow, nor do they predict the aspect ratio of the growing protrusions. Tikekar et al. also modeled lithium protrusion growth with solid electrolytes and determined the growth rate of protrusions as a function of their size.[26] They predict that protrusions wider than a certain critical diameter would grow spontaneously in height under applied electric fields. The peak growth rate was found to occur for protrusions with diameters slightly greater than the critical diameter.

Most experimental studies on the stability of lithium metal anodes focus on determining the effect of electrolyte design on the number of cycles to failure of lithium-lithium symmetric cells.[12,27–31] In contrast, this study presents data on the diameters and heights of growing lithium protrusions. We use a solid block copolymer electrolyte: polystyrene-*block*-poly(ethylene oxide) (SEO) mixed with lithium bis(trifluoromethanesulfonyl)imide (LiTFSI). Hard X-ray microtomography was used to quantify the nature of lithium protrusions.[13,28,30–35] We find that the short-circuiting protrusion is the one with the largest diameter, and that diameter scales linearly with electrolyte thickness. All the protrusions with lower heights, i.e. non-shorting protrusions, have smaller diameters. In addition, the heights of the protrusions are proportional to the protrusion diameter. Our experiments indicate that the fastest-growing protrusion has the largest diameter, a result that is counterintuitive and inconsistent with the existing theories. This motivated us to develop a new theory that builds upon existing models,[19,20,23,36] but goes beyond the elastic limits of the solid electrolyte and lithium metal. At sufficiently large stress, solids

undergo plastic deformation, wherein a small increase in stress leads to a very large increase in strain. Plastic deformation in metals is attributed to the movement of dislocations,[37] while that in block copolymers is attributed to reorientation of the local morphology.[38] The growth of lithium protrusions is affected by both local current density which adds to the volume of the protrusion, and the resulting stresses imposed by the solid electrolyte which can lead to plastic deformation of the protrusion. The counterintuitive experimental result arises due to these two effects.

Experimental Section

Materials. The polystyrene-b-poly(ethylene oxide) (SEO) diblock copolymer in this study was prepared by anionic polymerization, as described in previous work.[35] The polymer is denoted SEO(MPS-MPEO), where MPS and MPEO are the number-averaged molecular weights of PS and PEO, respectively, in kg mol^{-1}. Table 1 describes the relevant properties of the polymer used in this study, where ϕ_{EO} refers to the volume fraction of PEO. The self-assembled morphology of the block copolymer is expected to be lamellar based on the PEO volume fraction.

Table 1: Properties of SEO polymer used in this study: name, molecular weight of the PS block, molecular weight of the PEO block, volume fraction PEO of the neat polymer, and polydispersity index.

Name	M_{PS} [kg mol^{-1}]	M_{PEO} [kg mol^{-1}]	φ_{EO}	PDI
SEO(200-222)	200	222	0.51	1.08

Methods for electrolyte preparation and electrochemical cell fabrication mimics those previously reported by Maslyn et al.[35] All electrolyte preparation and lithium cell assembly was carried out in an Argon-filled glovebox with less than 1 ppm H_2O and less than 1 ppm O_2.

Electrolyte preparation. The SEO block copolymer was dissolved in anhydrous *N*-methylpyrrolidone (NMP, Sigma Aldrich) and mixed with lithium bis(trifluoromethane)

sulfonimide (LiTFSI) salt (Sigma Aldrich) such that the molar ratio of lithium ions to ethylene oxide groups was 0.085. An electrolyte film was then drop cast with a nickel-foil-coated solvent caster forming a sheet after the NMP evaporated away after 12 hours at 60 °C. The formed membrane was then further dried in the glovebox antechamber under active vacuum at 90 °C for at least 48 hours. Dried electrolytes films with a nominal thickness of 30 μm were brought inside the glovebox where all the cell assembly took place.

Li-SEO-Li symmetric cell assembly for cycling and tomographic imaging. A 7/16-inch diameter metal punch was used to cut polymer electrolyte discs from the cast films described above. For some cells, two or three of these discs were stacked and annealed together between fluorinated ethylene propylene liners in a hand-press at 120 °C for 10 minutes. Lithium metal foil was purchased from FMC Lithium at 99.9% purity. The foil thickness was 150 μm. Three to five layers of lithium metal foil were stacked on top of a piece of nickel foil, and then pressed until flat and shiny inside pouch material with a pneumatic press (130 MPa). The lithium electrodes were made by using a 3/8-inch diameter punch to cut through the layers of lithium foil and nickel foil backing. Two of these electrodes were used to sandwich the polymer electrolyte discs. The electrolyte thickness covered in this study ranged from 27 to 86 μm. Two 0.25 mm thick stainless steel shims were placed above and beneath the cell to fix the geometry of the cell. Aluminum current collector tabs were then affixed to the stainless steel shims and the sample was vacuum sealed in polypropylene-lined aluminum pouch material. Pouched cells were annealed for 12 hours at 120 °C before conducting electrochemical experiments.

Conditioning and Polarization. Cells were galvanostatically cycled or polarized at 90 °C in an Associated Environmental Systems SD-402 oven using a Maccor Series 4000 Battery Tester.

The cells were conditioned by galvanostatic cycling for 15 cycles at a low current density (0.02 mA cm^{-2}) as described by Maslyn et al.[35] Each cycle consisted of 4h of 0.02 mA cm^{-2} polarization in one direction, followed by 45 min of rest, then 4h of mA cm^{-2} polarization in the opposite direction, followed by 45 min of rest. After the conditioning cycles were completed, cells were polarized at a constant current density of 0.175 mA cm^{-2}. Cell failure was marked by a sudden drop in voltage.

X-ray microtomography. Hard X-ray microtomography was performed at Beamline 8.3.2 at the Advanced Light Source at Lawrence Berkeley National Laboratory. The cells were imaged before and after polarization using the methods and apparatus described by Maslyn et al.[35] Each cell was imaged in its entirety using a 2× lens, resulting in a tomogram with a pixel size of approximately 3.25 μm. About 76% of the cell volume was imaged in this configuration. The shorting protrusion was identified and the region in the vicinity of this protrusion was imaged again using a 4× lens, resulting in a tomogram with a pixel size of approximately 1.62 μm. About 19% of the cell volume was image in this configuration. Our analysis of the non-shorting protrusions is based on 2× lens data, while that of the shorting protrusion is based on the 4× lens data. Electrolyte thickness, *L*, reported in this study corresponds to the average distance between electrodes measured with ImageJ on the tomograms at 20 points within the cell before polarization. The reported error bars reflect the standard deviation of the values of *L* recorded from a given cell. Reconstructed three-dimensional (3D) images were analyzed using the commercially available Avizo software package.

Computational Section

Electrodeposition of lithium in a lithium-SEO-lithium symmetric cell was modeled using previously developed frameworks.[21,36] The equations of mass and charge balance, and mechanical equilibrium relations are solved in a two-dimensional rectangular coordinate frame to estimate the stress distribution at the electrode-electrolyte interface.[34,36] The list of the governing equations (GE), initial conditions (IC), and boundary conditions (BC) are provided in Table 2. The effect of mechanical stress on current density has been taken into consideration through the modified Butler-Volmer current expression (i_{BV}):[19,20]

$$i_{BV} = F\, k_{ref}\, c_e^{0.5} \exp\text{¿¿}. \qquad (1)$$

Here, F is the Faraday constant, k_{ref} indicates the reaction rate constant, c_e indicates the electrolyte salt concentration at the Li|SEO interface, $\Delta\mu_{e^-}$¿ is the stress-induced electrochemical potential, R is the universal gas constant, T is temperature, and η_s is the surface overpotential that is defined as, $\eta_s = \phi_s - \phi_e - U_{Li}$+¿, where, ϕ_s is the potential in the Li electrode, ϕ_e is the potential in the electrolyte, and U_{Li} is the open circuit potential of the cell, 0.0 V. During lithium deposition, in the absence of stress ($\Delta\mu_{e^-}$=0¿), i_{BV} is negative due to reducing overpotential that is negative in sign. The magnitude and sign of the stress induced electrochemical potential $\Delta\mu_{e^-}$¿ depends on the stress distribution at the electrode-electrolyte interface.[19,20] While estimating the stress distribution, elastic and plastic deformation of lithium and electrolyte is considered.[23,25,36] In the present analysis, both the working electrode and the counter electrode are modeled. The list of parameters used in the calculations are listed in Table 3. The dependence of these parameters on salt concentration is ignored. The salt concentration chosen (r = 0.085) is close to the concentration at which conductivity is maximized. A previous study has shown that transference number with respect to the solvent velocity exhibits complex behavior in the

vicinity of this salt concentration.[40] As shown by Villaluenga et al., $t^0_{+,SEO}$ is close to zero at r = 0.085. This implies that the presence of complex ion-clusters in the electrolyte and the transport of ions across the electrolyte is dominated by diffusion rather than migration.

Table 2. List of equations used in the computational analysis and some relevant boundary conditions.

GEs, BCs or ICs	Lithium electrode	SEO electrolyte
GE for charge balance	$\vec{\nabla}\cdot\left(\kappa_{Li}\vec{\nabla}\phi_{Li}\right)=0$	$\vec{\nabla}\cdot\left(\kappa_{SEO}\vec{\nabla}\phi_{SEO}\right)-\vec{\nabla}\cdot\left(\kappa_{D,SEO}\nabla\ln c_e\right)=0$ $\kappa_{D,SEO}=\left(\frac{2RT\kappa_{SEO}}{F}\right)\left(1-t_{+,SEO}\right)\left(1+\left(\frac{d\ln f_{\pm}}{d\ln c_e}\right)\right)$
BC at top and bottom	$-\kappa_{Li}\vec{\nabla}\phi_{Li}\big\|_{y=0}=-I_{app}$ $-\kappa_{Li}\vec{\nabla}\phi_{Li}\big\|_{y=L_y}=I_{app}$	$-\left(\kappa_{SEO}\vec{\nabla}\phi_{SEO}-\kappa_{D,SEO}\nabla\ln c_e\right)\big\|_{Li\vee SEO,top}=i_{BV,top}$ $-\left(\kappa_{SEO}\vec{\nabla}\phi_{SEO}-\kappa_{D,SEO}\nabla\ln c_e\right)\big\|_{Li\vee SEO,bottom}=i_{BV,bottom}$
GE for mass balance	--	$\frac{\partial c_e}{\partial t}=\vec{\nabla}\cdot\left(D_e\vec{\nabla}c_e\right)$
BC for mass balance	--	$-D_e\vec{\nabla}c_e\big\|_{Li\vee SEO,top}=\left(\left(1-t_{+,SEO}\right)/F\right)\cdot i_{BV,top}$ $-D_e\vec{\nabla}c_e\big\|_{Li\vee SEO,bottom}=-\left(\left(1-t_{+,SEO}\right)/F\right)\cdot i_{BV,bottom}$
IC for mass balance	--	$c_e(x,y,t=0)=c_{e,0}$
GE for stress equilibrium	$\vec{\nabla}\cdot\acute{\sigma}_{Li}=0$	$\vec{\nabla}\cdot\acute{\sigma}_{SEO}=0$
BC for stress equilibrium	$(u_x,u_y)\big\|_{y=0,L_y}=0$, $(u_x,u_y,f_x,f_y)\big\|_{Li\vee SEO}\rightarrow bc$	$(u_x,u_y,f_x,f_y)\big\|_{Li\vee SEO\,interface}\rightarrow balanced$

Governing equations, GE, Boundary conditions, BC, and Initial Conditions, IC.

Table 3. List of parameters used for running the simulations.

Name	Symbol	Unit	Value	Reference
Conductivity of SEO	κ_{SEO}	S/m	6.0×10^{-2}	39
Conductivity of Li	κ_{Li}	S/m	1.1×10^{7}	11
Transference number of SEO	$t^{0}_{+,SEO}$	--	0.0	40
Universal gas constant	R	$J/mol\cdot K$	8.314	--
Temperature	T	K	363	--
Faraday constant	F	C/mol	96485	--
Thermodynamic factor	$1+\left(\frac{d\ln f_{\pm}}{d\ln c_e}\right)$	--	2.5	40
Salt diffusivity in SEO	D_e	m^2/s	4.0×10^{-12}	40
Initial salt concentration	$c_{e,0}$	mol/m^3	1660	--
Reaction rate constant	k_{ref}	$\left(mol/m\cdot s^2\right)^{0.5}$	9.8×10^{-6}	36,39
Shear modulus of Li	G_{Li}	GPa	3.4	20
Poisson's ratio of Li	v_{Li}	--	0.42	20
Shear modulus of SEO	G_{SEO}	MPa	20.0	12
Poisson's ratio of SEO	v_{SEO}	--	0.33	20,34
Yield strength of Li	$\sigma_{0,Li}$	MPa	0.7	25
Yield strength of SEO	$\sigma_{0,SEO}$	MPa	3.0	Fitted

Results and Discussion

Figure 1a shows typical voltage versus time data obtained during galvanostatic polarization. After preconditioning cycles and 1 h of equilibration at 90 ºC, a current density of i = 0.175 mA cm^{-2} was imposed on the cell. The resulting voltage is shown in Figure 1a (solid black line). A sudden drop in voltage is observed at t = 35.1 h, indicating cell failure. We define cell lifetime as the time at which the sudden drop in voltage is observed. The charge passed before failure, C_d, is calculated using the imposed current density and time of failure, which for the cell in Figure 1a was 21.5 C cm^{-2}. All cells were polarized until failure by short circuit. The cell potentials changed by an average of 20% (9 mV) prior to the signature of cell failure. The

experiment described in Figure 1a was repeated on a total of 9 cells for electrolyte thicknesses ranging from 27 to 86 μm, and the results are shown in Figure 1b on a plot of C_d versus electrolyte thickness, L. It is evident that C_d increases with L. The dashed line is a least-squares fit through the data, forced through the origin. The slope of this line is 2.58×10^4 C cm^{-3}, and the data exhibit significant scatter away from the line. One expects longer lifetimes in cells with larger electrolyte thicknesses, as lithium protrusions have to grow across larger distances. The data in Figure 1b are consistent with that expectation. The values of C_d can be used to estimate the average thickness of the plated lithium layer, $t_{Li,calc} = C_d * 1.347 \times 10^{-4}$ cm^3 C^{-1}. This represents the thickness of the electrodeposited layer if the deposition were perfectly uniform across the cell.

Figure 1. Data obtained from galvanostatically polarized lithium-SEO-lithium symmetric cells. (a) A typical voltage versus time profile, taken from the cell with electrolyte thickness, L = 27 μm. The dashed line gives the applied current density, i, and the solid line gives the voltage response, V. The arrow indicates the time of cell failure, which is used to calculate charge passed before failure, C_d. (b) Plot of C_d as a function of L. C_d generally increases with L but exhibits significant scatter. The error bars correspond to variations in L across the cell. Detailed analysis is conducted on cells represented by black symbols.

The tomograms obtained from failed cells were examined manually to determine and examine the lithium protrusion that caused the short circuit. Two examples are shown in Figure 2. The images are shown with the electrode that was stripped on the top. In Figure 2a we show the side view (xz plane) of a small portion of the failed cell with $L = 27 \pm 2$ μm. Toward the left

and right edges of the figure, we see the bright band of SEO electrolyte sandwiched between the two lithium electrodes. The darker phase is lithium. In the middle of the figure, we see a globular lithium structure extending from the lower electrode to the upper electrode. This is the globule that caused the short circuit in the cell; no other protrusion spanned the distance between the two electrodes. The globule is surrounded by a polymeric sac that appears bright. The globule nucleates on an impurity particle in the electrode where lithium is electrodeposited. It is evident that the short circuit only occurs after the globule deforms both electrodes. The height of the globule is significantly larger than the thickness of the electrolyte. The nominal location of the electrode where deposition takes place is shown by a yellow dashed line in Figure 2a. A slice through the system in the xy plane along the dashed line is shown in Figure 2b. The particular protrusion that shorted this cell comprises two globules separated by a thin polymeric sac. A 3D volume rendering of this cell in the vicinity of the globule is shown in Figure 2c. Our objective is to visualize the 3D shape of the shorting globule. A convenient way to do this is to visualize the polymer sac. Dark voxels beyond a certain threshold are rendered transparent, while the bright voxels representing the polymer are rendered orange. The brighter voxels in the tomogram are mapped onto brighter voxels in the 3D rendering. Figure 2c thus emphasizes the electrolyte layer and the shorting globule. Note that the thin polymeric sac that is imaged directly conformally coats the shorting globule. Figures 2d, 2e, and 2f are analogous to Figures 2a, 2b, and 2c for the shorting globule in the cell with $L = 86 \pm 3$ μm, respectively. The top view of this globule (Figure 2e) indicates that the cross-section of the globule is more or less circular. For simplicity, we use the term protrusion to describe the non-planar lithium deposits in our cells regardless of

whether they contain one or two globules. The shorting protrusion in Figures 2a-c is significantly smaller than that shown in Figures 2d-f.

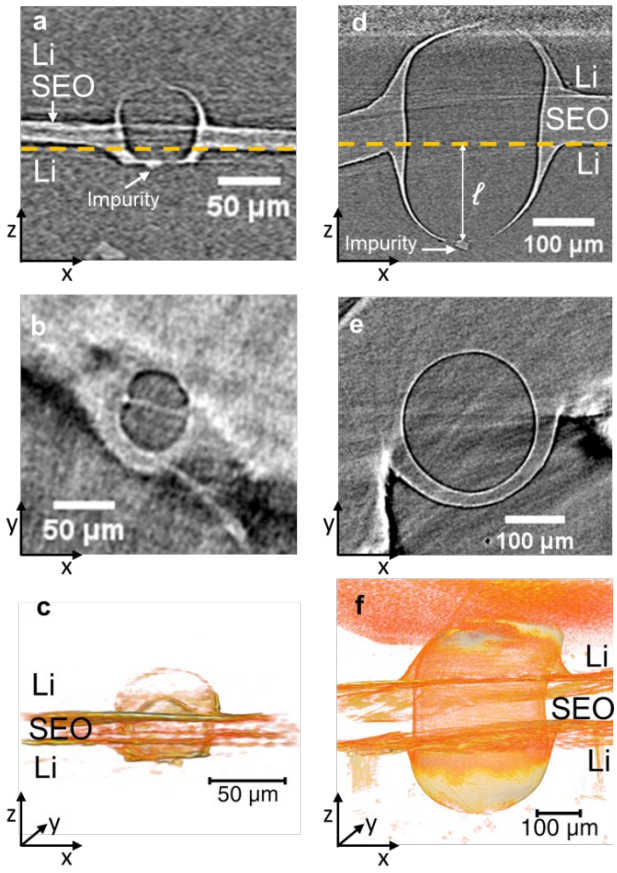

Figure 2. Examples of shorting lithium protrusions observed by X-ray tomography in cells with electrolyte thickness L = 27 µm (left column) and 86 µm (right column). The top row shows an orthogonal cross-section through the cell and the protrusion. The bottom electrode is where plating takes place. The orange dotted line indicates the plane corresponding to the bottom electrode-electrolyte interface. Roughly speaking, the impurity marks the initial location of the electrode-electrolyte interface. This plane is used to measure ℓ, the distance between the nucleating impurity particle and the bottom electrode-electrolyte interface. A top-view of this plane is shown in the middle row. The bottom row shows a 3D rendered volume that includes the

protrusions. (a) Cross-section in the xz plane of shorting lithium protrusion in the failed cell with L = 27 μm. (b) Cross-section of the xy plane of the protrusion shown in panel (a). (c) Volume rendering of the defect shown in panels (a) and (b). (d) Cross-section in the xz plane of shorting protrusion in the failed cell with L = 86 μm. (e) Cross-section in the xy plane of the defect shown in panel (d). (f) Volume rendering of the defect shown in panels (d) and (e).

The shape of the protrusion is complex, with cross-sectional area that varies significantly with z. We use two length scales to characterize the shape of the protrusion. The slice through the bottom electrode-electrolyte interface (e.g. Figures 2b,e) is used to determine the characteristic diameter of the protrusion, d. We first determine the cross-sectional area of the protrusion at this interface, A, and define $d = 2\sqrt{A/\pi}$. We define a vertical length, ℓ, as the distance between the nucleating impurity particle and the bottom electrode-electrolyte interface. The electrode-electrolyte interface is not perfectly flat near the protrusions, and thus there is some uncertainty in the definition of that interface. We estimate the error to be 2 μm. The values of A, d, and ℓ of the shorting protrusions in five of the cells presented in Figure 1b were thus determined and the results are presented in Table 4.

Table 4 gives values of parameters C_d, voltage at time of failure V_s, calculated average thickness of the plated lithium layer $t_{Li,calc}$, ℓ, A, and d of the shorting protrusion as a function of L. It is evident that neither C_d nor ℓ are clearly correlated to L. For example, a small change in L from 27 ± 2 μm to 33 ± 2 μm results in an increase in C_d from 21.5 to 153.4 C cm^{-2}. In Figure 3a we plot ℓ as a function of L. Figure 3b shows the side view of the shorting protrusion in the cell with L = 33 μm. (Moving forward, we leave out the error bars for brevity.) This protrusion is much longer than the one that shorted the L = 33 μm cell. There is a clear correlation between C_d

and ℓ in the L = 33 μm cell. Note that these parameters are determined independently: C_d is obtained from the potentiostat, while ℓ is determined from X-ray tomography. The X-ray tomography data provides an explanation for the large difference in cell lifetime when L is changed from 27 to 33 μm. Most of the shorting protrusion in the L = 33 μm cell is buried inside the bottom lithium electrode. For reasons that are unclear, the protrusion formed in the L = 33 μm cell grows for a considerable amount of time without reaching the top electrode. It appears that cell failure depends on numerous parameters that are difficult to predict.

In most cases, ℓ is less than $t_{Li,calc}$, suggesting that the nucleation of the protrusion did not occur at t = 0. The only exception is the L = 33 μm cell, which exhibited an extremely tall protrusion that was mostly buried in the bottom electrode (Figure 3b). We posit that this is due to an increase in the local current density in the vicinity of the protrusion.

Table 4: Properties of the Short-circuiting Protrusions in Failed Cells as a function of Electrolyte Thickness.

L [μm]	C_d [C cm^{-2}]	$t_{Li,calc}$ [μm]	V_s [mV]	ℓ [μm]	A [μm]	d_s [μm]
27 ± 2	21.5	29	16.6	11.0	2900	61
33 ± 2	153.4	207	28.9	269	5250	82
51 ± 3	181.9	245	73.5	193	14800	137
77 ± 3	172.2	232	99.3	128	22700	170.
86 ± 3	205.9	277	53.6	154	40100	226

Cell Lifetime, C_d, Voltage just before Time of Failure, $t_{Li,calc}$, Calculated Average Thickness of Lithium, V_s, Distance of Nucleating Impurity Particle to Bottom Electrode-Electrolyte Interface, ℓ, Cross-sectional Area, A, and Area-based Diameter, d.

Figure 3. (a) Plot of distance between the nucleating impurity particle and the bottom electrode-electrolyte interface, ℓ, versus electrolyte thickness, L, in failed cells. Plating occurs at the bottom electrode. (b) Orthogonal cross-section through the cell and the short-circuiting lithium globule observed by X-ray tomography in the failed cell with L = 33 μm. The orange dotted line

indicates the plane corresponding to the bottom electrode-electrolyte interface. This protrusion is unusually long and resides almost entirely within the bottom electrode. Compare this with the protrusion shown in Figure 1a for L = 27 μm.

It is evident in Table 4 that both A and d increase systematically with increasing L. In Figure 4, we plot d versus L for the shorting protrusions. To a good approximation, d is linearly proportional to L. The dashed line has a slope of 2.47 ± 0.29 and is a least-squares fit through the origin. The square of the correlation coefficient, R^2, for the fit is 0.946. To a reasonable approximation, the d versus L dependence can be described by a straight line that goes through the origin. Note that the diameters of the shorting protrusions in the L = 27 and 33 μm cells are similar in spite of the large difference in ℓ.

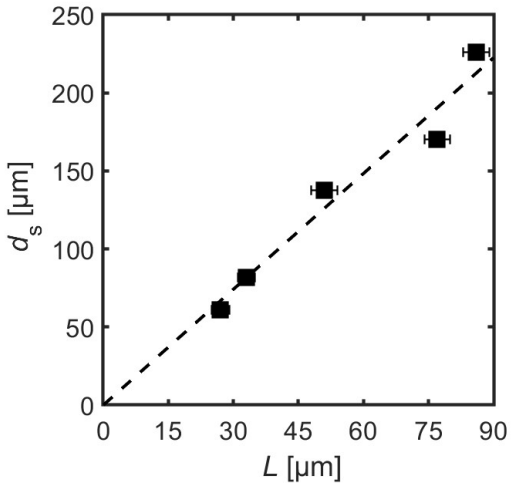

Figure 4. Plot of diameter, d_s, of short-circuiting protrusions in failed cells as a function of electrolyte thickness, L. The equation for the dashed line is d_s = 2.47 L [μm]. The uncertainty in slope is ± 0.29.

Thus far we have focused on the shorting protrusions. We manually examined the X-ray tomograms of the cells with L = 51 and 86 μm and determined the diameter of 29 and 23 visible

protrusions, respectively. In Figure 5a, we show an example of a non-shorting protrusion in the cell with L = 86 μm. The height of each protrusion, h, is defined as the distance from the bottom electrode-electrolyte interface to the upper tip of the protrusion. The height of the particular protrusion shown in Figure 5a is marked on the figure. In Figure 5b, we plot d versus h for all of the non-shorting protrusions in the selected cells. The shorting protrusions are demarcated by filled symbols, where h is taken to be L. As seen in Figure 2, the growth of the shorting protrusions results in plastic deformation of the lithium metal as it extends into the top electrode. In contrast, the non-shorting protrusions cause plastic deformation of the polymer electrolyte. By assuming $h = L$, we acknowledge that the processes leading to the deformation of the top electrode are fundamentally different from those leading to the growth of the protrusions into the polymer electrolyte. The observation that the characteristics of the shorting protrusions are consistent with the characteristics of the non-shorting protrusions.

The data in Figure 5b suggests that d/L of the shorting protrusion can be estimated from the d/h dependence of non-shorting protrusions. The cells contained a wide variety of protrusions covering a range of diameters from 35 to 225 μm and heights ranging from 7 to 86 μm. In spite of the large variation, all of the data are consistent with a linear fit, as shown by a dashed line in Figure 5b. The slope of the linear fit, $\Delta d/\Delta h$, is 2.39 ± 0.12. This correlation indicates that wider protrusions extend further into the electrolyte. The intercept of the linear fit in Figure 5b is 22.4 ± 2.6 μm. The R^2 of the fit is 0.972. It appears that only structures with diameters above this critical length scale protrude into the electrolyte.

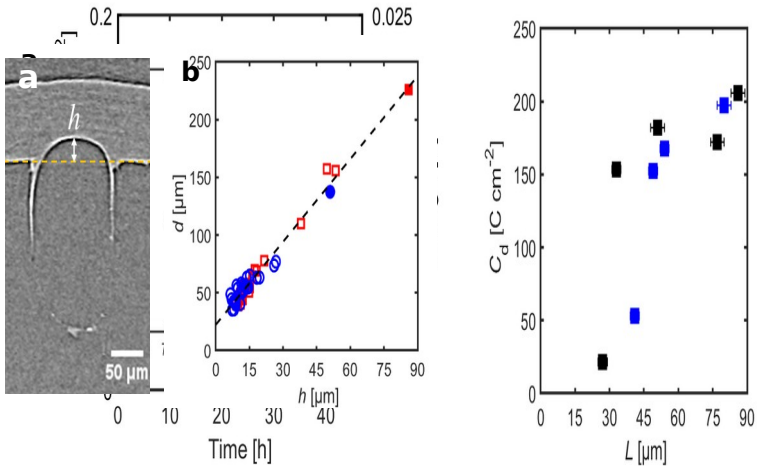

Figure 5. (a) Orthogonal cross-section through the cell and a non-shorting lithium protrusion observed by X-ray tomography in the failed cell with L = 86 µm. The height, h, is measured between the bottom electrode-electrolyte interface to the upper tip of the globule. The bottom electrode is the plating electrode. (b) Plot of diameter, d, versus distance through electrolyte, h, for protrusions in cells with electrolyte thicknesses L = 51 and 86 µm. Blue circles represent protrusions in the L = 51 µm cell, while red squares represent those in the L = 86 µm cell. Protrusions responsible for short-circuiting the cell are indicated by filled symbols, and the h given for these protrusions is assumed to be the electrolyte thickness for the cell. The equation for the dashed line is $d = 2.39\ h + 22.4$ [µm]. The uncertainties in slope and intercept are ± 0.12 and ± 2.6 µm, respectively.

In Figure 6, we plot the local diameter, d_z, of the shorting protrusion as a function of position, z, for cells with L = 33 and 86 µm. For this analysis, the position z is defined with respect to the nucleating impurity particle, and the protrusion diameter is obtained from the cross-sectional area at that position. The range of z is 0 to ℓ. We are thus focusing on the portion of the protrusion that is buried within the bottom electrode. In the case of the L = 86 µm cell, shown in

the inset, the diameter of the shorting protrusion increases rapidly until z = 96 μm, and then remains constant at a value that is approximately d_s. In the case of the L = 33 μm cell, shown in Figure 4b, the diameter of the shorting protrusion increases slowly before reaching a short plateau at $z \approx$ 250 μm, at a value that is approximately d_s.

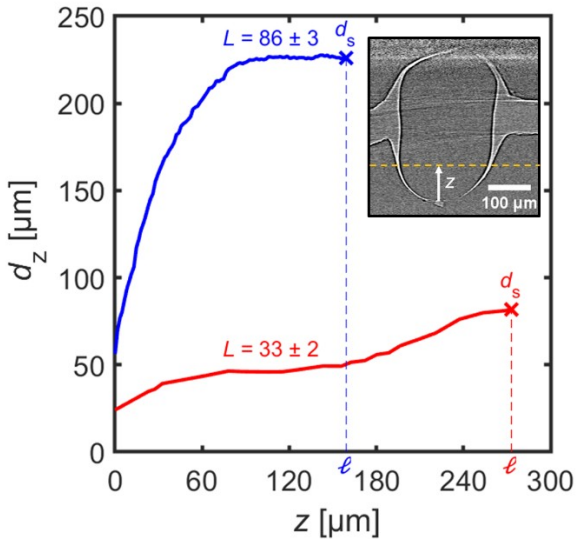

Figure 6. Diameter d_z of short-circuiting protrusion as a function of vertical distance, z, from the nucleating impurity particle. The range of z is from 0 to ℓ, the distance from the nucleating impurity particle to the bottom electrode-electrolyte interface. The plane indicated by the yellow dotted line in the inset is used to measure d_z of the short-circuiting protrusion within the L = 86 μm cell. The short-circuiting protrusion in the L = 33 μm cell corresponding to the red line is shown in Figure 4b.

The computational model described above was used to elucidate the underpinnings of our experimental observations. The competition between growth of the protrusion height and that of the protrusion diameter was determined using the following steps:

1. Protrusions similar to those used in References [20], [22] and [36] with prescribed h and d were generated. A sinusoidal shape of the protrusions (defined as a half sine wave from $\frac{\pi}{2}$ to $\frac{3\pi}{2}$) was preferred over the capsule shapes observed experimentally due to the continuous geometry and ease of computational implementation. An example of the computational domain is shown in Figure 7a. The Li ions are assumed to flow from the top to the bottom of the electrolyte.
2. The current distribution at the bottom electrode-electrolyte interface was determined using the methodology outlined in the computation section.
3. The total amount of Li deposition at the bottom electrode was determined from Faraday's law.
4. The planar top electrode-electrolyte interface was moved upward according to the total amount of deposition. The electrolyte is pushed upward, and this results in a loss of contact between the bottom electrode and the electrolyte.
5. The electrolyte is then pushed downward to bring the bottom electrode and electrolyte back in contact. Plastic deformation of Li, from the tip of the protrusion to the valley, occurs during this last step, which can lead to increase in protrusion diameter.

From this final configuration that is in mechanical equilibrium, the change in the protrusion height, Δh, and the increase in the protrusion diameter, Δd, is determined. This analysis is repeated for different values of h, d, and L. We report results of three sets of simulations: (1) varying d at constant h = 8 μm and L = 26 μm, (2) varying L at constant h = 15 μm and d = 39 μm, and (3) varying h at constant d/h = 2.4 and L = 26, 52, 78, and 104 μm. We refer to these as Simulation 1, 2, and 3. In the present analysis, for electrolyte thickness of L = 26 μm, the size of each mesh was assumed to be 1 μm × 1 μm, which means $\Delta x = \Delta z$ = 1 μm, where Δx and Δz are the dimensions of the mesh along the x and z directions (Figure 7a). For thicker electrolytes,

where, L = 52, 78, and 104 μm, larger values of $\Delta x = \Delta z$ = 2, 3, and 4 μm were adopted, respectively. Such variable mesh sizes were adopted to keep the computational analysis tractable within a reasonable amount of time even with thicker electrolytes.

The initial and final configurations of one protrusion are shown in Figure 7b by the black and magenta lines, respectively. The change in height Δh and change in diameter Δd, during lithium deposition, is shown explicitly in the same figure. The change in height and diameter of the protrusion is measured at two specific locations, near the peak and valley, respectively, ignoring complexities of Li deposition at other locations. Δh is measured at the tip (x = 0 μm), and Δd is measured one mesh point above the valley of the protrusion, which is around z = 27 μm for the particular protrusion geometry shown in Figure 7b. There are three factors that can contribute to the increase in protrusion diameter: a) stress-induced current at the valley, b) plastic deformation of lithium, and c) interfacial curvature effects.[19,20,23,25,36,41] Since the sizes of the protrusions are on the range of microns, interfacial curvature effects are negligible[20] and thus ignored in our calculations.

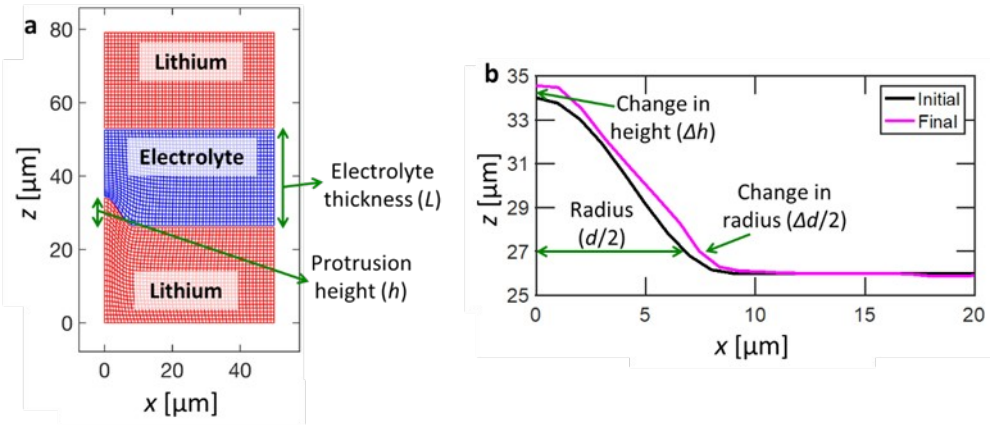

Figure 7. (a) Geometry of the model for the lithium-SEO-lithium cell. The mesh used for the finite element calculations is shown here. The stripping electrode is shown on the top, and the

plating electrode with a protrusion is shown at the bottom. (b) An example of the lithium-SEO boundary in the vicinity of the protrusion, showing the initial boundary and the final boundary after deposition predicted by modeling. Change in height, Δh, and change in diameter, Δd, are shown in the figure, which were measured at the tip (x = 0 μm) and one mesh point above the valley of the protrusion (z = 27 μm), respectively.

To understand the impact of stress-induced electrochemical potential, $\Delta \mu_{e^-}$, on Δh, both $\Delta \mu_{e^-}$ and Δh at the peak $(x=0)$ are plotted in Figure 8 with respect to d. L and h have been kept constant in this simulation at 26 and 8 μm, respectively (Simulation 1). Figure 8 shows that increasing d reduces ¿¿, and this increases the magnitude of the Li^+ current at the peak (see Equation 1). This results in an increase in Δh. It can also be concluded from Figure 8 that protrusions with larger diameter will grow more rapidly in height. This is consistent with the experimental observation that the shorting protrusion had the largest diameter.

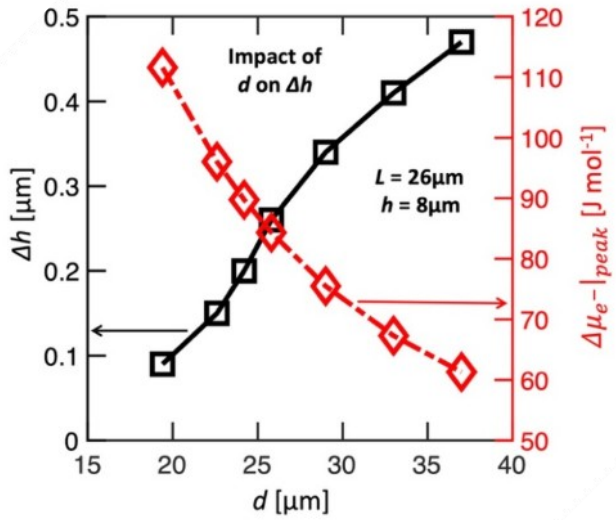

Figure 8. The effect of protrusion diameter, d, on the increase in protrusion height, Δh, (left y-axis, black squares) and the stress-induced electrochemical potential at the peak (x = 0), ¿¿ (right y-axis red diamonds). These calculations were conducted at constant L (26 μm) and h (8 μm).

Figure 9a plots vertical stress versus x for various values of L. The height and diameter of the protrusion are kept constant at h = 15 μm and d = 39 μm, respectively (Simulation 2). It is evident that the region near the peak of the protrusion (x = 0 μm) experiences compression, whereas the region close to the valley (x = 19 μm) experiences tension. The compressive stress at the peak decreases with increasing L, while the magnitude of the tensile stress at the valley initially increases, and then decreases, with increasing L. Decrease in the stress with increasing L can be attributed to the fact that with increasing L, the ratio h/L decreases, which leads to a drop in strain experienced by the electrolyte.

In Figure 9b, we plot Δd and $\Delta \mu_{e^-}$ at the valley as a function of L. Note that ¿¿ is negative because the mechanical stress is tensile, and this stress can be relieved by increasing the Li^+ current at the valley. In addition, we also calculated the ratio of the current densities at the protrusion peak over the valley $\left(i_{peak}/i_{valley}\right)$. This ratio was 0.83, 0.66, 0.74 and 0.8 for L = 26, 52, 78 and 104 μm, respectively, and it mirrors the dependence of ¿¿ as a function of L. Current ratio $\left(i_{peak}/i_{valley}\right)$ less than unity indicates that more lithium is electrodeposited at the valley. Δd increases monotonically with L (left y-axis), but ¿¿ exhibits a minimum at L = 52 μm (right y-axis). The increase in ¿¿ with increasing L beyond the maximum is due to a reduction in electrolyte strain, which in turn reduces electrolyte stress. The increase in Δd at L < 52 μm can be attributed to an increase in Li^+ current in the valley; i_{peak}/i_{valley} decreases from 0.83 to 0.66 as L is increased from 26 to 52 μm. However, the increase in Δd at L > 52 μm cannot be due to the same effect, because i_{peak}/i_{valley} increases from 0.66 at L = 52 μm to 0.74 and 0.8 for L = 78 and 104 μm, respectively. The increase in Δd observed when L is increased from 52 to 104 μm is due to plastic deformation of lithium metal. The increase in Δd with L seen in Figure 9b is consistent

with the experimental observation that the shorting protrusion diameter increases with L (Figure 4).

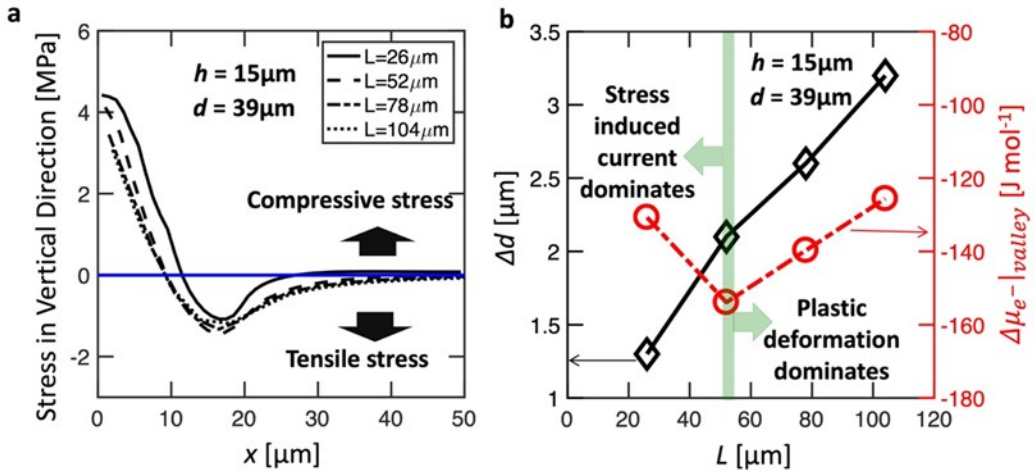

Figure 9. (a) Vertical stress along the lithium-SEO boundary as a function of x. Tensile stress in the valley in the vicinity of x = 19 µm results in an increased current density at that location. (b) The effect of electrolyte thickness, L, on the increase in protrusion diameter Δd (left y-axis, black diamonds) and the magnitude of stress-induced electrochemical potential at the valley, ¿¿ (right y-axis, red circles). Calculations in (a) and (b) were conducted at constant protrusion diameter, d (39 µm), and height, h (15 µm). The effect of plastic deformation of lithium on Δd increases with increasing L.

Simulations were conducted for a variety of protrusions heights, h, between 8 and 86 µm, the same range covered by experiments. The ratio d/h was kept constant at 2.4 (Simulation 2 and 3). In Figure 10, we plot $\Delta d/\Delta h$ as a function of h. This ratio is remarkably constant over a wide range of protrusion heights and electrolyte thicknesses. The yield strength of the SEO electrolyte has not yet been measured. In the simulations we adjusted this value to 3.0 MPa to force agreement between the theoretical $\Delta d/\Delta h$ and the experimentally determined slope of d versus h

in Figure 5b. The noise in the simulation results is attributed to the complex geometry of the time-dependent electrode-electrolyte interface (Figure 7b). The simulations provide support for the observed linear dependence of d versus h. A complete model of the growth of lithium protrusions from nucleation to short-circuit is outside the scope of this paper (and all other theoretical work in this field). Developing such a model will require additional information such as the non-linear viscoelastic properties of the block copolymer electrolyte and effects of the solid electrolyte interphase (SEI). It must also account for the concentration dependence of the ion transport properties of the electrolyte.

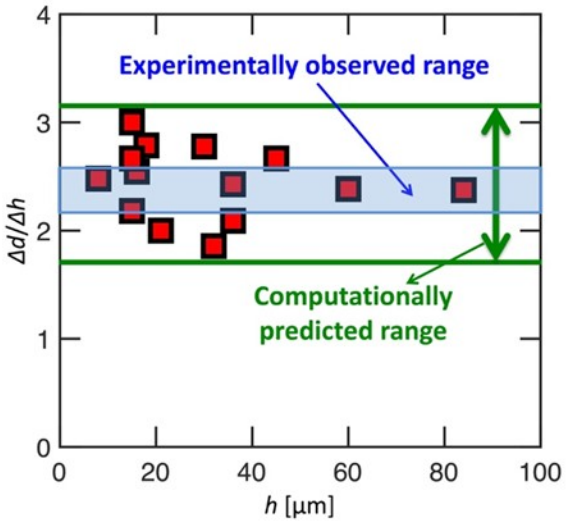

Figure 10. Computational predictions of the ratio $\Delta d/\Delta h$ characterizing the growth of lithium protrusions as a function of protrusion height, h. The experimentally determined slope of d versus h, 2.39 ± 0.12, is also shown. The yield strength of SEO was used as a fitting parameter to obtain a match between computation and experiment.

Conclusion

Lithium protrusion growth in lithium-SEO-lithium symmetric cells was studied by X-ray microtomography. Cells with varying electrolyte thicknesses ranging from 27 to 86 μm were polarized at a constant current density of i = 0.175 mA cm^{-2} until a short circuit was observed. The cell lifetime was not a monotonic function of electrolyte thickness. However, we observed that the diameter of the shorting protrusion increased linearly with electrolyte thickness. We also observed a linear correlation between the height and diameter of all visible protrusions. This correlation was applicable to protrusions that did not grow all the way to the stripping electrode, as well as the short-circuiting protrusions. A model that accounted for both elastic and plastic deformation of the electrolyte and the electrode was used to establish the underpinnings of our observations. The electrochemical properties of the SEO electrolyte dictate the rate at which lithium is deposited on a simulated protrusion. The increase in protrusion diameter is dictated by stress-induced current at low values of electrolyte thickness (below 52 μm), while it is dictated by plastic deformation of lithium metal at high values of electrolyte thickness (above 52 μm). The ratio $\Delta d/\Delta h$ obtained in simulations is insensitive to changes in protrusion height and electrolyte thickness. Simulations indicate that a narrow and sharp protrusion is characterized by a large stress-induced electrochemical potential at the peak, which leads to a reduction in current density at the peak, and this suppresses its growth. In contrast, a broad protrusion is characterized by a smaller stress-induced electrochemical potential at the peak, which leads to a smaller reduction in current density at the peak, and this promotes its growth. Both simulations and experiments indicate that protrusions with a broad range of diameters grow in symmetric cells, but counterintuitively, the fastest-growing protrusions have the largest diameters.

Acknowledgements

This work was primarily supported by the Vehicle Technologies Office of the U.S. Department of Energy's Office of Energy Efficiency and Renewable Energy under the guidance of the Advanced Battery Cell Research Program (eXtreme fast charge Cell Evaluation of Lithium-ion batteries, XCEL). Hard X-ray experiments were performed at the Advanced Light Source, which is supported by the Director, Office of Science, Office of Basic Energy Sciences, of the U.S. Department of Energy under Contract No. DE-AC02-05CH11231. Jacqueline A. Maslyn was supported by a National Science Foundation Graduate Research Fellowship DGE-2752814. Whitney S. Loo was supported by a National Science Foundation Graduate Research Fellowship DGE-1106400. Louise Frenck was supported by the Energy and Biosciences Institute through the EBI-Shell program. Pallab Barai and Venkat Srinivasan were supported by Vehicle Technologies Office (VTO), Department of Energy (DOE), USA, under Contract No. DE-AC02-05CH11231 under the Battery Materials Research (BMR) program. Argonne National Laboratory is operated for DOE Office of Science by UChicago Argonne, LLC under the contract number DE-AC02-06CH11357.

List of Symbols

Symbol	Description	Unit
A	Cross-sectional area of shorting protrusion	μm^2
C_d	Charge passed before failure	C cm^{-2}
d	Area-based diameter	µm
d_s	Area-based diameter of shorting protrusion	µm
d_z	Area-based diameter at a position z away from the nucleating impurity particle	µm
h	Height, measured from the bottom electrode-electrolyte interface to the upper tip of the protrusion	µm
i_{peak}	Current density at the peak of the protrusion	mA cm^{-2}
i_{valley}	Current density at the valley of the protrusion	mA cm^{-2}
ℓ	Distance from the nucleating impurity particle to the bottom electrode-electrolyte interface	µm
L	Electrolyte thickness	µm
$t_{Li,calc}$	Calculated Average Thickness of Lithium	µm
V_s	Voltage just before time of failure	V
Δd	Change in diameter	µm
Δh	Change in height	µm
$\Delta \mu_{e^-}$	Stress-induced electrochemical potential	J mol^{-1}
¿¿	Stress-induced electrochemical potential at the peak of the protrusion	J mol^{-1}
¿¿	Stress-induced electrochemical potential at the valley of the protrusion	J mol^{-1}

References

(1) Balsara, N. P.; Newman, J. Comparing the Energy Content of Batteries, Fuels, and Materials. *J. Chem. Educ.* **2013**, *90* (4), 446–452. https://doi.org/10.1021/ed3004066.

(2) Albertus, P.; Babinec, S.; Litzelman, S.; Newman, A. Status and Challenges in Enabling the Lithium Metal Electrode for High-Energy and Low-Cost Rechargeable Batteries. *Nat. Energy* **2018**, *3* (1), 16–21. https://doi.org/10.1038/s41560-017-0047-2.

(3) Tarascon, J. M.; Armand, M. Issues and Challenges Facing Rechargeable Lithium Batteries. *Nature* **2001**, *414* (6861), 359–367. https://doi.org/10.1038/35104644.

(4) Selim, R.; Bro, P. Some Observations on Rechargeable Lithium Electrodes in a Propylene Carbonate Electrolyte. *J. Electrochem. Soc.* **1974**, *121* (11), 1457. https://doi.org/10.1149/1.2401708.

(5) Epelboin, I.; Froment, M.; Garreau, M.; Thevenin, J.; Warin, D. Behavior of Secondary Lithium Ad Aluminium-Lithium Electrodes in Propylene Carbonate. *Proc. - Electrochem. Soc.* **1980**, *80–4*, 417–442. https://doi.org/10.1149/1.2129354.

(6) Lin, D.; Liu, Y.; Cui, Y. Reviving the Lithium Metal Anode for High-Energy Batteries. *Nat. Nanotechnol.* **2017**, *12* (3), 194–206. https://doi.org/10.1038/nnano.2017.16.

(7) Yamaki, J.; Tobishima, S.; Hayashi, K.; Keiichi Saito; Nemoto, Y.; Arakawa, M. A Consideration of the Morphology of Electrochemically Deposited Lithium in an Organic Electrolyte. *J. Power Sources* **1998**, *74* (2), 219–227. https://doi.org/10.1016/S0378-7753(98)00067-6.

(8) Aurbach, D. A Short Review of Failure Mechanisms of Lithium Metal and Lithiated Graphite Anodes in Liquid Electrolyte Solutions. *Solid State Ionics* **2002**, *148* (3–4), 405–416. https://doi.org/10.1016/S0167-2738(02)00080-2.

(9) Rao, B. M. L.; Electrochem, J. Lithium - Aluminum Electrode Lithium-Aluminum Electrode. **1977**, *124*, 1490–1492.

(10) Takeda, Y.; Yamamoto, O.; Imanishi, N. Lithium Dendrite Formation on a Lithium Metal Anode from Liquid, Polymer and Solid Electrolytes. *Electrochemistry* **2016**, *84* (4), 210–218. https://doi.org/10.5796/electrochemistry.84.210.

(11) Monroe, C.; Newman, J. Dendrite Growth in Lithium/Polymer Systems. *J. Electrochem. Soc.* **2003**, *150* (10), A1377. https://doi.org/10.1149/1.1606686.

(12) Stone, G. M.; Mullin, S. A.; Teran, A. A.; Hallinan, D. T.; Minor, A. M.; Hexemer, A.; Balsara, N. P. Resolution of the Modulus versus Adhesion Dilemma in Solid Polymer Electrolytes for Rechargeable Lithium Metal Batteries. *J. Electrochem. Soc.* **2012**, *159* (3), A222–A227. https://doi.org/10.1149/2.030203jes.

(13) Schauser, N. S.; Harry, K. J.; Parkinson, D. Y.; Watanabe, H.; Balsara, N. P. Lithium Dendrite Growth in Glassy and Rubbery Nanostructured Block Copolymer Electrolytes. *J. Electrochem. Soc.* **2015**, *162* (3), A398–A405. https://doi.org/10.1149/2.0511503jes.

(14) Khurana, R.; Schaefer, J. L.; Archer, L. A.; Coates, G. W. Suppression of Lithium Dendrite Growth Using Cross-Linked Polyethylene/Poly(Ethylene Oxide) Electrolytes: A New Approach for Practical Lithium-Metal Polymer Batteries. *J. Am. Chem. Soc.* **2014**,

136 (20), 7395–7402. https://doi.org/10.1021/ja502133j.

(15) Liu, K.; Pei, A.; Lee, H. R.; Kong, B.; Liu, N.; Lin, D.; Liu, Y.; Liu, C.; Hsu, P.; Bao, Z.; Cui, Y. Lithium Metal Anodes with an Adaptive "Solid-Liquid" Interfacial Protective Layer. *J. Am. Chem. Soc.* **2017**, *139* (13), 4815–4820. https://doi.org/10.1021/jacs.6b13314.

(16) Lopez, J.; Pei, A.; Oh, J. Y.; Wang, G. J. N.; Cui, Y.; Bao, Z. Effects of Polymer Coatings on Electrodeposited Lithium Metal. *J. Am. Chem. Soc.* **2018**, *140* (37), 11735–11744. https://doi.org/10.1021/jacs.8b06047.

(17) Porz, L.; Swamy, T.; Sheldon, B. W.; Rettenwander, D.; Frömling, T.; Thaman, H. L.; Berendts, S.; Uecker, R.; Carter, W. C.; Chiang, Y. M. Mechanism of Lithium Metal Penetration through Inorganic Solid Electrolytes. *Adv. Energy Mater.* **2017**, *7* (20), 1–12. https://doi.org/10.1002/aenm.201701003.

(18) Yu, S.; Schmidt, R. D.; Garcia-Mendez, R.; Herbert, E.; Dudney, N. J.; Wolfenstine, J. B.; Sakamoto, J.; Siegel, D. J. Elastic Properties of the Solid Electrolyte Li7La3Zr2O12 (LLZO). *Chem. Mater.* **2016**, *28* (1), 197–206. https://doi.org/10.1021/acs.chemmater.5b03854.

(19) Monroe, C.; Newman, J. The Effect of Interfacial Deformation on Electrodeposition Kinetics. *J. Electrochem. Soc.* **2004**, *151* (6), 880–886. https://doi.org/10.1149/1.1710893.

(20) Monroe, C.; Newman, J. The Impact of Elastic Deformation on Deposition Kinetics at Lithium/Polymer Interfaces. *J. Electrochem. Soc.* **2005**, *152* (2), 396–404. https://doi.org/

10.1149/1.1850854.

(21) Newman, J.; Thomas-Alyea, K. E. Electrochemical Systems. 2004, Hoboken. New Jersey: John Wiley & Sons, Inc.

(22) Barai, P.; Higa, K.; Srinivasan, V. Effect of Initial State of Lithium on the Propensity for Dendrite Formation : A Theoretical Study. *J. Electrochem. Soc.* **2017**, *164* (2), 180–189. https://doi.org/10.1149/2.0661702jes.

(23) Barai, P.; Higa, K.; Srinivasan, V. Impact of External Pressure and Electrolyte Transport Properties on Lithium Dendrite Growth. *J. Electrochem. Soc.* **2018**, *165* (11), A2654–A2666. https://doi.org/10.1149/2.0651811jes.

(24) Liu, G.; Lu, W. A Model of Concurrent Lithium Dendrite Growth, SEI Growth, SEI Penetration and Regrowth. *J. Electrochem. Soc.* **2017**, *164* (9), A1826–A1833. https://doi.org/10.1149/2.0381709jes.

(25) LePage, W. S.; Chen, Y.; Kazyak, E.; Chen, K.-H.; Sanchez, A. J.; Poli, A.; Arruda, E. M.; Thouless, M. D.; Dasgupta, N. P. Lithium Mechanics: Roles of Strain Rate and Temperature and Implications for Lithium Metal Batteries. *J. Electrochem. Soc.* **2019**, *166* (2), A89–A97. https://doi.org/10.1149/2.0221902jes.

(26) Tikekar, M. D.; Archer, L. A.; Koch, D. L. Stabilizing Electrodeposition in Elastic Solid Electrolytes Containing Immobilized Anions. *Sci. Adv.* **2016**, *2* (7). https://doi.org/10.1126/sciadv.1600320.

(27) Hallinan, D. T.; Mullin, S. A.; Stone, G. M.; Balsara, N. P. Lithium Metal Stability in

Batteries with Block Copolymer Electrolytes. *J. Electrochem. Soc.* **2013**, *160* (3), 464–470. https://doi.org/10.1149/2.030303jes.

(28) Devaux, D.; Harry, K. J.; Parkinson, D. Y.; Yuan, R.; Hallinan, D. T.; MacDowell, A. A.; Balsara, N. P. Failure Mode of Lithium Metal Batteries with a Block Copolymer Electrolyte Analyzed by X-Ray Microtomography. *J. Electrochem. Soc.* **2015**, *162* (7), A1301–A1309. https://doi.org/10.1149/2.0721507jes.

(29) Markevich, E.; Salitra, G.; Chesneau, F.; Schmidt, M.; Aurbach, D. Very Stable Lithium Metal Stripping-Plating at a High Rate and High Areal Capacity in Fluoroethylene Carbonate-Based Organic Electrolyte Solution. *ACS Energy Lett.* **2017**, *2* (6), 1321–1326. https://doi.org/10.1021/acsenergylett.7b00300.

(30) Maslyn, J. A.; Frenck, L.; Loo, W. S.; Parkinson, D. Y.; Balsara, N. P. Extended Cycling through Rigid Block Copolymer Electrolytes Enabled by Reducing Impurities in Lithium Metal Electrodes. *ACS Appl. Energy Mater.* **2019**, *2* (11), 8197–8206. https://doi.org/10.1021/acsaem.9b01685.

(31) Frenck, L.; Maslyn, J. A.; Loo, W. S.; Parkinson, D. Y.; Balsara, N. P. Impact of Salt Concentration on Nonuniform Lithium Electrodeposition through Rigid Block Copolymer Electrolytes. *ACS Appl. Mater. Interfaces* **2019**, *11* (51), 47878–47885. https://doi.org/10.1021/acsami.9b15606.

(32) Harry, K. J.; Hallinan, D. T.; Parkinson, D. Y.; MacDowell, A. A.; Balsara, N. P. Detection of Subsurface Structures underneath Dendrites Formed on Cycled Lithium Metal Electrodes. *Nat. Mater.* **2014**, *13* (1), 69–73. https://doi.org/10.1038/nmat3793.

(33) Harry, K. J.; Liao, X.; Parkinson, D. Y.; Minor, A. M.; Balsara, N. P. Electrochemical Deposition and Stripping Behavior of Lithium Metal across a Rigid Block Copolymer Electrolyte Membrane. *J. Electrochem. Soc.* **2015**, *162* (14), A2699–A2706. https://doi.org/10.1149/2.0321514jes.

(34) Harry, K. J.; Higa, K.; Srinivasan, V.; Balsara, N. P. Influence of Electrolyte Modulus on the Local Current Density at a Dendrite Tip on a Lithium Metal Electrode. *J. Electrochem. Soc.* **2016**, *163* (10), A2216–A2224. https://doi.org/10.1149/2.0191610jes.

(35) Maslyn, J. A.; Loo, W. S.; McEntush, K. D.; Oh, H. J.; Harry, K. J.; Parkinson, D. Y.; Balsara, N. P. Growth of Lithium Dendrites and Globules through a Solid Block Copolymer Electrolyte as a Function of Current Density. *J. Phys. Chem. C* **2018**, *122*, acs.jpcc.8b06355. https://doi.org/10.1021/acs.jpcc.8b06355.

(36) Barai, P.; Higa, K.; Srinivasan, V. Lithium Dendrite Growth Mechanisms in Polymer Electrolytes and Prevention Strategies. *Phys. Chem. Chem. Phys.* **2017**, *19* (31), 20493–20505. https://doi.org/10.1039/c7cp03304d.

(37) Lemaitre, J.; Chaboche, J.-L. *Mechanics of Solid Materials*; Cambridge university press, 1994.

(38) Haenelt, T. G.; Georgopanos, P.; Abetz, C.; Rangou, S.; Alisch, D.; Meyer, A.; Handge, U. A.; Abetz, V. Morphology and Elasticity of Polystyrene-Block-Polyisoprene Diblock Copolymers in the Melt. *Korea Aust. Rheol. J.* **2014**, *26* (3), 263–275. https://doi.org/10.1007/s13367-014-0031-3.

(39) Wu, S.-L.; Javier, A. E.; Devaux, D.; Balsara, N. P.; Srinivasan, V. Discharge Characteristics of Lithium Battery Electrodes with a Semiconducting Polymer Studied by Continuum Modeling and Experiment. *J. Electrochem. Soc.* **2014**, *161* (12), A1836–A1843.

(40) Villaluenga, I.; Pesko, D. M.; Timachova, K.; Feng, Z.; Newman, J.; Srinivasan, V.; Balsara, N. P. Negative Stefan-Maxwell Diffusion Coefficients and Complete Electrochemical Transport Characterization of Homopolymer and Block Copolymer Electrolytes. *J. Electrochem. Soc.* **2018**, *165* (11), A2766–A2773. https://doi.org/10.1149/2.0641811jes.

(41) Bucci, G.; Christensen, J. Modeling of Lithium Electrodeposition at the Lithium/Ceramic Electrolyte Interface: The Role of Interfacial Resistance and Surface Defects. *J. Power Sources* **2019**, *441*, 227186.

Graphic for manuscript